crystals

MDPI

Article

Synthesis of Silver Nanocubes@Cobalt Ferrite/Graphitic Carbon Nitride for Electrochemical Water Splitting

Ausrine Zabielaite *, Olegas Eicher-Lorka, Zenonas Kuodis, Ramunas Levinas, Dijana Simkunaite, Loreta Tamasauskaite-Tamasiunaite * and Eugenijus Norkus

Center for Physical Sciences and Technology (FTMC), LT-10257 Vilnius, Lithuania; olegas.eicher-lorka@ftmc.lt (O.E.-L.); zenonas.kuodis@ftmc.lt (Z.K.); ramunas.levinas@ftmc.lt (R.L.); dijana.simkunaite@ftmc.lt (D.S.); eugenijus.norkus@ftmc.lt (E.N.)

* Correspondence: ausrine.zabielaite@ftmc.lt (A.Z.); loreta.tamasauskaite@ftmc.lt (L.T.-T.)

Abstract: This study presents the synthesis of graphitic carbon nitride (g-C_3N_4) and its nanostructures with cobalt ferrite ($CoFe_2O_4$) and silver nanocubes (Ag) when using the combined pyrolysis of melamine and the polyol method. The resulted nanostructures were tested as electrocatalysts for hydrogen and oxygen evolution reactions in alkaline media. It was found that Ag@$CoFe_2O_4$/g-C_3N_4 showed the highest current density and gave the lowest overpotential of −259 mV for HER to reach a current density of 10 mA cm^{-2} in a 1 M KOH. The overpotentials for reaching the current density of 10 mA·cm^{-2} for OER were 370.2 mV and 382.7 mV for Ag@$CoFe_2O_4$/g-C_3N_4 and $CoFe_2O_4$/g-C_3N_4, respectively. The above results demonstrated that $CoFe_2O_4$/g-C_3N_4 and Ag@$CoFe_2O_4$/g-C_3N_4 materials could act as bifunctional catalysts due to their notable performances and high stabilities toward hydrogen and oxygen evolution reactions (HER and OER). Total water splitting in practical applications is a promising alternative to noble-metal-based electrocatalysts.

Keywords: graphitic carbon nitride; silver nanocubes; cobalt ferrite; polyol method; hydrogen; oxygen; evolution

check for updates

Citation: Zabielaite, A.; Eicher-Lorka, O.; Kuodis, Z.; Levinas, R.; Simkunaite, D.; Tamasauskaite-Tamasiunaite, L.; Norkus, E. Synthesis of Silver Nanocubes@Cobalt Ferrite/Graphitic Carbon Nitride for Electrochemical Water Splitting. *Crystals* **2023**, *13*, 1342. https://doi.org/10.3390/cryst13091342

Academic Editor: Mauro Francesco Sgroi

Received: 28 July 2023
Revised: 27 August 2023
Accepted: 30 August 2023
Published: 2 September 2023

Copyright: © 2023 by the authors. Licensee MDPI, Basel, Switzerland. This article is an open access article distributed under the terms and conditions of the Creative Commons Attribution (CC BY) license (https://creativecommons.org/licenses/by/4.0/).

1. Introduction

The development of green hydrogen production technologies by water electrolysis (water splitting) has become one of the major current priorities [1–7]. Large-scale green H_2 ecosystems are highly desirable, but challenging to implement. The development of green H_2 ecosystems is severely constrained by limitations such as the relatively low production and storage efficiencies of renewable technologies; purification; and high transportation and utilization costs (which include safety concerns regarding the handling of H_2 [8]). Green hydrogen production via the renewable method of water electrolysis ($2H_2O \rightarrow 2H_2 + O_2$, E° = 1.23 V vs. RHE) can result in pure H_2 and O_2 without carbon emissions, and it is based on the OER and HER taking place at the anode and cathode, respectively [1,3,8]. The main challenge is to design and develop novel, non-noble, and low-cost bifunctional electrode materials with high efficiency for both HER and OER. It is also important to address the environmental impact of engineered nanomaterials and the difficulty of recovering them, as well as the possibility of recycling, regeneration, and reuse [9]. Transition-metal boride/phosphide-based materials are attractive catalysts for H_2 release due to their advantages of being earth-abundant elements, as well as their considerable catalytic activity, high stability, and low cost [10]. Metal nanoparticles as catalysts have also attracted a great deal of attention over the last few decades owing to their unique properties. However, due to their high surface energy, metal nanoparticles tend to aggregate into clumps and eventually into their bulk counterparts, resulting in reduced catalytic activity and long-term stability. Dispersing or anchoring the metal nanoparticles onto certain supporting materials with a large surface area to form a supported catalyst

can improve the stability of the catalyst by averting the aggregation of nanoparticles. Therefore, selecting suitable supports is crucial for obtaining stable and catalytically active catalysts. So far, many supporting materials (metal oxides, organic polymer, porous materials, carbon-based materials, etc.) have been broadly investigated to stabilize metal nanoparticles. Recently, g-C_3N_4 has been widely used as a base carrier for the deposition of nanoparticles of various metals (Ni, Co, Mn, Cu, Fe, etc.) and their oxides. G-C_3N_4 has excellent properties, such as a high bulk modulus, good thermal conductivity, a small mechanical friction coefficient, high elasticity, and chemical inertness. Moreover, g-C_3N_4 is also a very promising material that can replace the commonly used carbon for the production of catalysts due to its high nitrogen (N) content. Among the many carbon-based materials, g-C_3N_4 has great potential in various photocatalytic and electrocatalytic applications due to its tunable physicochemical and electrical properties, as well as its non-toxic and metal-free nature, as well as its visible light optical response, environmental friendliness, biocompatibility, etc. [11–25]. Currently, there is a strong scientific interest in the polymeric g-C_3N_4 as a photocatalyst given its outstanding characteristics, such as its 2D graphite planar structure and its tunable visible energy band gap of 2.7 eV (with a valence band maximum of 1.6 eV and a conduction band minimum of 1.1 eV vs. NHE, which allows for the absorption of visible light up to 460 nm in addition to the facile synthesis methods used [17,26–28]). This has led to its widespread use in the photocatalytic degradation of many environmental pollutants for the purposes of CO_2 reduction, bacterial disinfection, and the degradation of harmful organic substances [11,12,14,16,26]. Currently, a great deal of focus is on the photocatalytic production of H_2 via water splitting [26,27,29–37]. However, the practical application of g-C_3N_4 for photocatalytic hydrogen evolution is limited due to several drawbacks, including its high recombination rate of photogenerated electron–hole pairs, low surface area, low number of active sites, its limited absorption of light in the visible range of 460 only, its low movement of photogenerated charge carries, the slow kinetics of its surface reaction, its rapid backward and side reactions, the degree of dissolved oxygen, product separation, reproducibility, etc. [19,26–29,38].

Equally, due to the strong covalent bonds between the carbon and N atoms, g-C_3N_4 can effectively act as an electrocatalyst for water splitting, which is active for both OER and HER reactions [15,20,23]. However, the low conductivity and limited availability of redox sites limit the applicability of pristine g-C_3N_4 [19]. The production of g-C_3N_4 material is cheap and does not require high costs [14]. A simple approach to obtain g-C_3N_4 is the polymerization of cyanamide, dicyandiamide, or melamine [14,25,39–43]. Depending on the reaction conditions, different materials with different degrees of condensation, properties, and reactivities can be obtained [39]. In this study, g-C_3N_4 was synthesized with melamine as a precursor. Figure 1 presents the structure of melamine, which is a kind of three-triazine heterocyclic organic compound.

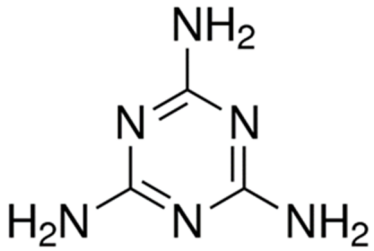


Figure 1. Structure of melamine.

Heating the melamine at different temperatures—depending on the respective thermal polymerization temperatures of 500, 520, and 540 °C [44]—allows for the different morphologies of g-C_3N_4 to be obtained, which range from nanosheets to rolled nanosheets, nanotubes, and nanoflakes with nanoparticles. These morphologies have different properties that can significantly affect the functionality of g-C_3N_4 [44]. However, the optimal use of g-C_3N_4 for electrochemical applications requires an improvement of its poor conduc-

tivity, which can be increased in several ways: physically mixing g-C_3N_4 with conductive carbon materials; immobilizing g-C_3N_4 on carbon bases (carriers) or depositing metal nanoparticles via microwave-assisted processes; hydrothermal and solvothermal syntheses routes; sol–gel processes; chemical reduction, etc. The application of earth-abundant transition/noble metal-free (TMs, where M = Co, Ni, Fe, Mn, Mo) and TM-based alloys or non-metallic (TMXs, where X = N, O, S, C, P, etc.) compounds as active electrocatalysts for HER/OER has been reported [45–49]. TMXs have received much attention due to their distinctive structural features, abundant active sites, tunable electronic properties, compositions, and ease of employment for large-scale production. Co, Ni, and Fe are typically characterized as the most powerful materials for water splitting [50–53]. Among them, Co-based electrocatalysts, including cobalt oxides [54], hydroxides [55], nitrides [56,57], sulfides [58], selenides [59], phosphides [60], and cobalt ferrite oxide [6,61,62], play a rather significant role in water splitting and are widely used in HER/OER [63,64]. However, their catalytic performance and stability do not yet meet the requirements for use in practical applications. Many electrocatalysts based on cobalt suffer from poor electrical conductivity and low-charge transfer efficiency [63,64]. Efficient and stable Co-based electrocatalytic materials with sufficient intrinsic electronic structure and an unlimited number of active sites on the surface for optimized water splitting remain challenging.

Recently, $CoFe_2O_4$ as a type of mixed valence transition metal oxide with spinel structure has received considerable attention due to its chemical stability, high coercivity, large saturation magnetization, mechanical hardness, as well as—most importantly—being a promising catalyst in terms of low cost, high catalytic activity, and environmental friendliness with excellent electrical conductivities [65,66]. This makes it suitable for use in applications such as catalysis, photocatalysis [65,67], supercapacitors [68], fuel cells [69], batteries [70], and many other areas. Although CoO and $CoFe_2O_4$ improve the performance of bare g-C_3N_4 in a variety of processes, including water oxidation, the activity required for practical applications has yet to be achieved [71]. Coupling with noble metal Ag nanoparticles is appropriate for overcoming insufficient catalytic activity. Ag nanoparticles have been extensively studied among metallic nanoparticles due to their versatility in synthesis, ease of processing, fast kinetic reaction rate, high thermal and chemical stability, good conductivity, etc. [14,72]. Recently, an eightfold increase in the catalytic activity of Co_2P by forming an Ag@Co_xP core–shell nanostructure for OER has been reported [72]. It was assumed that synergistic interactions between the Ag core and shell determine the OER as the Ag core modulates the electronic structure of Co_xP, thus leading to enhanced catalytic activity. The g-C_3N_4-decorated with $BiVO_4/Ag_2CO_3$ was investigated for HER and OER, and showed admirable activity and good stability for OER with a very low overpotential of 136 mV in an alkaline medium [73]. The outstanding activity of the electrocatalyst was attributed to the decoration and electronic interaction of g-C_3N_4 with the $BiVO_4/Ag_2CO_3$ nanocomposite, in which its surface area, active sites, and charge transfer were increased, and its resistance was decreased. Ag@$CoFe_2O_4$/g-C_3N_4 as a photocatalyst showed an improvement in unprecedented photocatalytic activity toward H_2 production [74]. The photocatalytic activity of the *p*-CFO/*n*-CN heterojunction was enhanced after adding Ag nanoparticles on the surface of photocatalysts via the formation of a plasmonic heterojunctions between Ag and CFO ($CoFe_2O_4$). This resulted in photocatalytic improvements by providing active sites for the adsorption of water molecules for the light-driven catalytic reactions that produced both H_2 and O_2.

Based on these findings, we reported the synthesis of $CoFe_2O_4$/g-C_3N_4 and silver nanocube Ag@$CoFe_2O_4$/g-C_3N_4 nanostructures with the polyol method, as well as their employment as electrocatalysts for HER and OER in alkaline media.

2. Materials and Methods

2.1. Materials and Synthesis

Melamine (99%); Fe(II) acetylacetonate ($C_{15}H_{24}FeO_6$, 99%); Co(II) acetylacetonate ($C_{10}H_{14}CoO_4$, 99%), $AgNO_3$ (99%); methanol (CH_3OH, 99%); tetra ethylene glycol (TEG);

$HO(CH_2CH_2O)_3CH_2CH_2OH$, 99%); polyvinylpyrrolidone (PVP); 1,5-pentanediol, potassium hydroxide (KOH, 98.8%); and Cu(II) chloride ($CuCl_2$, 99%) were purchased from Merck KGaA (Darmstadt, Germany) and used for the synthesis.

2.1.1. Synthesis of g-C_3N_4

Firstly, the g-C_3N_4 was prepared via the thermal annealing of melamine at a temperature of 520 °C for 4 h. The precursor was placed in a closed high-alumina crucible and heated to temperature with a rate of 5 °C/min. After the synthesis, it was ground into a fine powder.

2.1.2. Synthesis of $CoFe_2O_4$/g-C_3N_4 Nanoparticles Using the Polyol Method

A total of 0.112 mmol of $C_{15}H_{24}FeO_6$ and 0.056 mmol of $C_{10}H_{14}CoO_4$ were dissolved in 8 mL of TEG under ultrasonication. Then, 0.041 mmol of synthesized g-C_3N_4 was added to the reaction mixture. The scheme of the reaction mixture is shown in Figure 2.

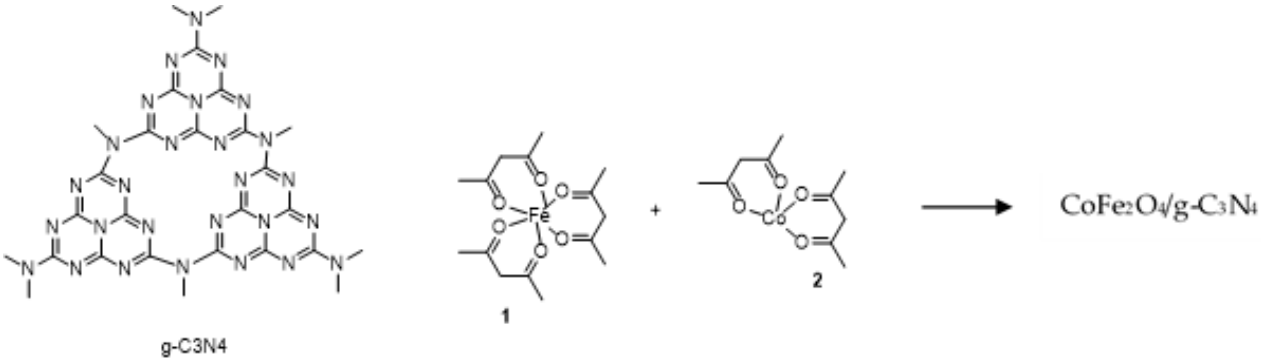


Figure 2. Scheme of the synthesis of $CoFe_2O_4$/g-C_3N_4.

The resultant mixture was kept in a "Monowave 300" microwave reactor (Anton Paar, Graz, Austria). Synthesis was carried out according to the following protocol: the temperature was increased to 180 °C within 2 min, followed by a temperature increase to 270 °C within 3 min. Then, the synthesis was carried out at 270 °C for 58 min. The reaction mixture during synthesis was stirred with a magnetic stirrer. The obtained product was washed four times with methanol, and the particles were separated with a neodymium magnet. The final colloid of nanoparticles was diluted with methanol to 1.5 mL.

2.1.3. Synthesis of Ag Nanocubes

Ag nanocubes were synthesized according to the procedure described in [75]. Briefly, 2.94 mmol of $AgNO_3$ and 0.0064 µmol of $CuCl_2$ were dissolved in 12.5 mL of 1,5-pentanediol. In a separate flask, 2.215 mmol of PVP was dissolved in 12.5 mL of 1,5-pentanediol. Using a temperature-controlled silicone oil bath, a reaction flask containing 20 mL of 1,5-pentanediol was heated to 175 °C and maintained for 10 min. Then, the two precursor solutions were injected into the hot reaction flask at different rates: 0.5 mL of the $AgNO_3$ solution every minute, and 0.25 mL of the PVP solution every 30 s. $AgNO_3$ was poured 7 times, PVP-14. The reaction was stopped by simply removing it from the heat source and waiting for it to cool down.

Additionally, methanol was added for dilution. Particles were deposited by centrifugation at 8000 rpm for 8 min. After deposition, the final product was washed with methanol 3 times by mixing the particles in an ultrasonic bath. The resulting nanoparticle colloid was diluted with methanol to 3 mL.

2.1.4. Ag@$CoFe_2O_4$/g-C_3N_4

To obtain Ag@$CoFe_2O_4$/g-C_3N_4, 250 µL of prepared $CoFe_2O_4$/g-C_3N_4 solution was mixed with 100 µL of a silver colloidal solution and then kept for at least one day with occasional stirring in an ultrasonic bath.

2.2. Characterization of Catalysts

The XRD patterns of the studied powders were measured using an X-ray diffractometer D2 PHASER (Bruker, Karlsruhe, Germany). The measurements were conducted in the 2θ range of 10–70°.

A transmission electron microscope Tecnai G2 F20 X-TWIN (FEI, Eindhoven, The Netherlands) was used to characterize catalyst shape and size.

The SEM images and distribution of elements in the catalysts were analyzed using a scanning electron microscope TM4000Plus with an AZetecOne detector (Hitachi, Tokyo, Japan).

2.3. Electrochemical Measurements

The performance of the synthesized samples was evaluated using a PGSTAT100 potentiostat/galvanostat (Metrohm Autolab B.V., Utrecht, The Netherlands). A standard three-electrode cell was used, where the working electrode was a glassy carbon (GC) electrode modified with the synthesized samples. The geometric surface area of the GC electrode was 0.196 cm^2. A Ag/AgCl (3 M KCl) and GC road were employed as the reference and counter electrodes, respectively. Linear sweep voltammograms (LSVs) were recorded in an N_2-saturated 1 M KOH solution at a scan rate of 2 mV s^{-1}. All reported potential values were referred to as "E_{RHE}"-reversible hydrogen electrode according to the following Equation (1):

$$E_{RHE} = E_{measured} + 0.059 \cdot pH + E_{Ag/AgCl\ (3\ M\ KCl)} \quad (1)$$

where $E_{Ag/AgCl\ (3M\ KCl)}$ = 0.210 V.

The current densities for HER and OER presented in this paper were normalized to the geometric area of the catalysts.

The stability tests of the $CoFe_2O_4$/g-C_3N_4 and Ag@$CoFe_2O_4$/g-C_3N_4 catalysts were conducted for 1000 cycles at a constant scan rate of 100 mV s^{-1} at a rotation speed of 1600 rpm, after which the stable polarization curves were recorded at 2 mV s^{-1} for comparison with the initial curve.

3. Results and Discussion

The structure of the synthesized $CoFe_2O_4$/g-C_3N_4 and Ag@$CoFe_2O_4$/g-C_3N_4 was examined by XRD. Figure 3 presents the XRD patterns of g-C_3N_4 (a), $CoFe_2O_4$/g-C_3N_4 (b), and Ag@$CoFe_2O_4$/g-C_3N_4 (c). The XRD pattern of the as-prepared g-C_3N_4 exhibited a typical pattern with a pronounced peak, which was centered approximately at 27.3° and had several small diffraction peaks at 13.2°, 18°, 22°, 44°, and 56.5° (Figure 3); this may be assigned to the (002), (100), (101), (111), (103), and (004) planes of the trigonal N bond of tri-s-triazine and the layered packing of the conjugated aromatic units in g-C_3N_4, respectively [44,76,77].

Strong diffraction peaks at the 2θ values of 27.6° were seen in both the XRD patterns of $CoFe_2O_4$/g-C_3N_4 and Ag@$CoFe_2O_4$/g-C_3N_4 indicating that the g-C_3N_4 structure had not changed (Figure 3b,c). The XRD pattern of $CoFe_2O_4$/g-C_3N_4 consisted of well-indexed peaks at 18.3°, 30.3°, 35.5°, 43.2°, 57.1°, and 62.2°, which corresponded to the (*h k l*) planes 111, 220, 311, 400, 511, and 440, respectively. These matched well with a cubic spinel phase of $CoFe_2O_4$ according to COD 1,533,163 (Figure 3b). The same peaks were also observed in the XRD pattern of Ag@$CoFe_2O_4$/g-C_3N_4 (Figure 3c). However, two characteristic diffraction peaks of Ag at 2θ values of 38.2° and 44.4° were seen in the XRD pattern for

Ag@$CoFe_2O_4$/g-C_3N_4 (Figure 3c). Those peaks corresponded to the 111 and 200 crystalline planes of Ag with a cubic symmetry (COD1509146).

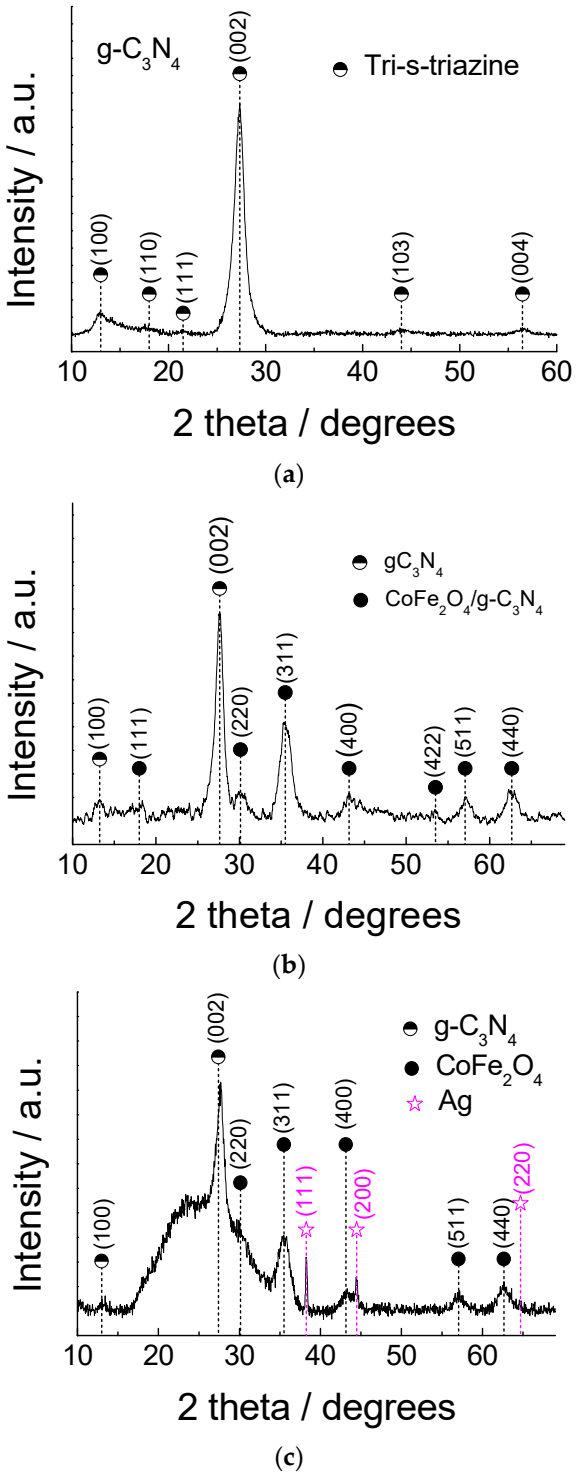


Figure 3. XRD patterns for the (**a**) g-C_3N_4, (**b**) $CoFe_2O_4$/g-C_3N_4, and (**c**) Ag@$CoFe_2O_4$/g-C_3N_4 catalysts.

The morphology of $CoFe_2O_4$/g-C_3N_4 and Ag@$CoFe_2O_4$/g-C_3N_4 was observed by SEM. The SEM images of both catalysts showed irregular spherical agglomerated particles of different sizes (Figures 4a and 5a). The EDS spectra for $CoFe_2O_4$/g-C_3N_4 (Figure 4b) and Ag@$CoFe_2O_4$/g-C_3N_4 (Figure 5b) confirmed the existence of metal species Co and Fe

on $CoFe_2O_4$/g-C_3N_4, as well as0 Co, Fe, and Ag on Ag@$CoFe_2O_4$/g-C_3N_4. The elemental mapped images of $CoFe_2O_4$/g-C_3N_4 (Figure 4c–e) and Ag@$CoFe_2O_4$/g-C_3N_4 (Figure 5c–f) showed a homogeneous distribution of Co, Fe, and O, as well as Co, Fe, O, and Ag, respectively, thus indicating the great uniformity of the synthesized $CoFe_2O_4$/g-C_3N_4 and Ag@$CoFe_2O_4$/g-C_3N_4.

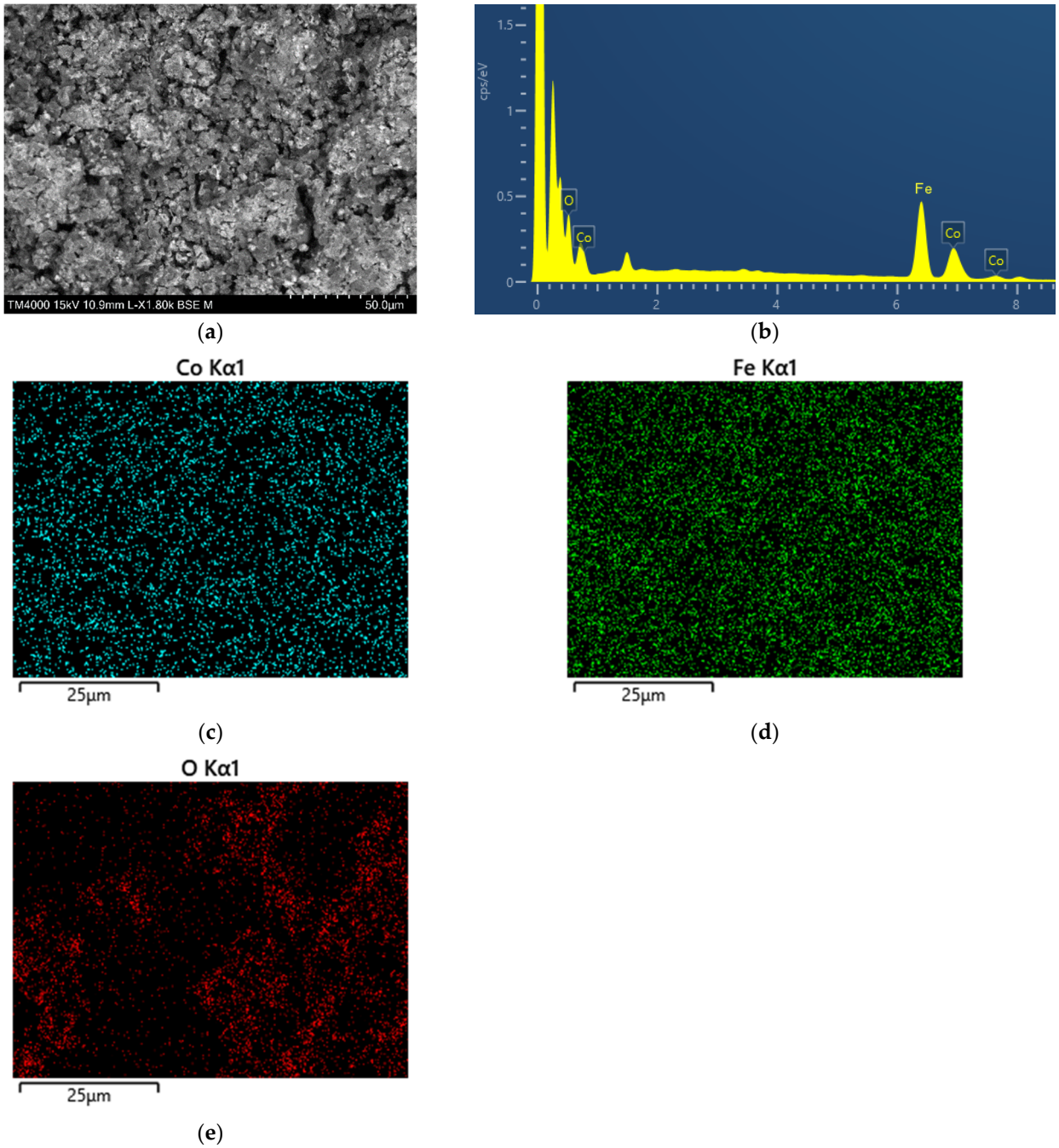


Figure 4. (**a**) SEM image and (**b**) corresponding EDS pattern of $CoFe_2O_4$/g-C_3N_4. (**c**–**e**) The elemental mapped images.

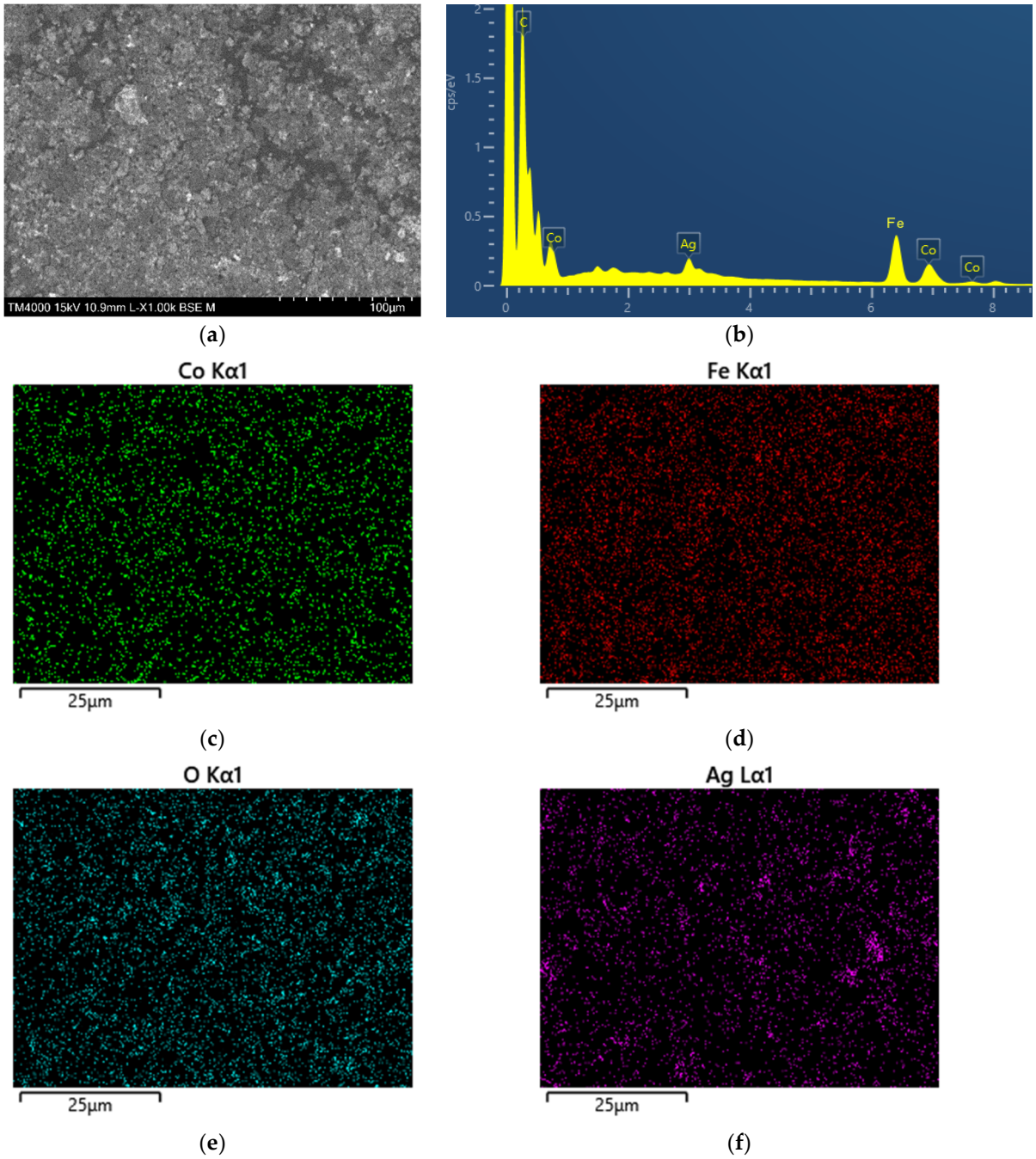


Figure 5. (**a**) SEM image and (**b**) corresponding EDS pattern of Ag@$CoFe_2O_4$/g-C_3N_4. (**c**–**f**) The elemental mapped images.

It can be seen from Figure 6 that Ag nanocubes with a size of 30–40 nm were loaded on the $CoFe_2O_4$/g-C_3N_4.

The electrocatalytic activity of the prepared catalysts was investigated for HER and OER in an alkaline medium. The HER polarization curves recorded on the g-C_3N_4, $CoFe_2O_4$/g-C_3N_4, and Ag@$CoFe_2O_4$/g-C_3N_4 samples in alkaline media are shown in Figure 7a, whereas the data of the electrochemical performance of the tested catalysts are given in Table 1.

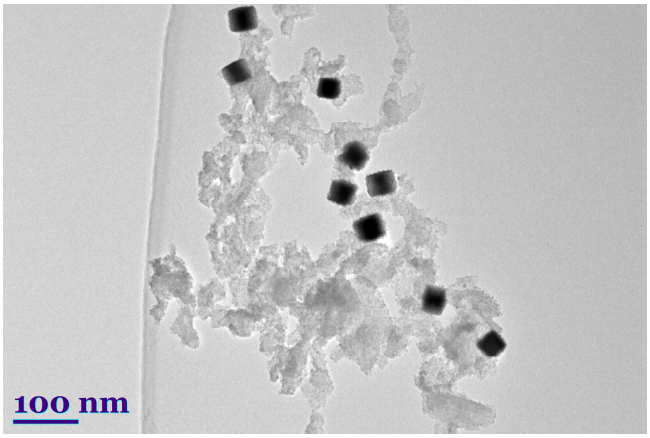


Figure 6. TEM image of the Ag@$CoFe_2O_4$/g-C_3N_4 catalyst.

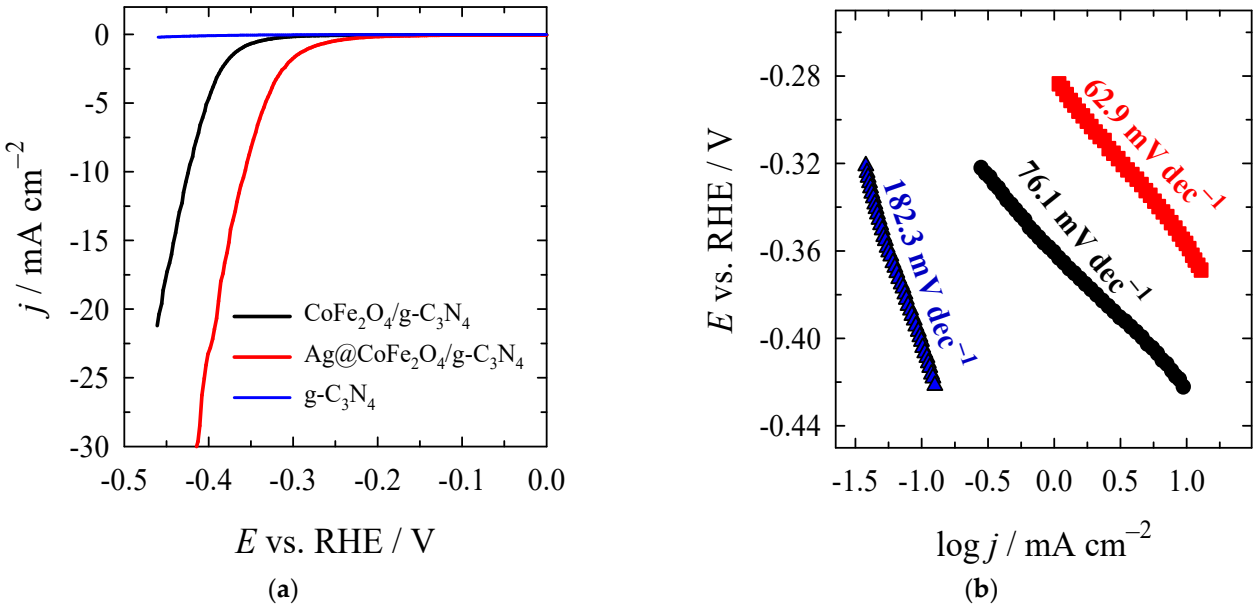


Figure 7. (**a**) HER polarization curves of the g-C_3N_4, $CoFe_2O_4$/g-C_3N_4, and Ag@$CoFe_2O_4$/g-C_3N_4 catalysts in a 1 M KOH solution at a potential scan rate of 2 mV s^{-1}. (**b**) The corresponding Tafel slopes for each catalyst.

Table 1. Electrochemical parameters of the investigated materials toward HER in alkaline media.

Sample	E_{onset}, V at j = −0.1 mA cm^{-2}	η_{10} *, mV	Tafel Slope, mV dec^{-1}
g-C_3N_4	−0.40	–	182.3
$CoFe_2O_4$/g-C_3N_4	−0.280	−424.6	76.1
Ag@$CoFe_2O_4$/g-C_3N_4	−0.161	−259.0	62.9

* Overpotential at 10 mA cm^{-2}.

As shown in Table 1, the Ag/$CoFe_2O_4$/g-C_3N_4 sample exhibited the lowest onset potential (E_{onset}) of −0.161 V for the HER when compared with $CoFe_2O_4$/g-C_3N_4 and pure g-C_3N_4. Additionally, the latter catalyst showed a significantly higher current density and a lower overpotential of −259.0 mV for the HER to reach a current density of 10 mA cm^{-2} (η_{10}) (Figure 5a) when compared to that of $CoFe_2O_4$/g-C_3N_4 (−424.6 mV).

The reaction kinetics and mechanism of the as-prepared catalysts can be evaluated on the basis of Tafel slopes, which were determined from the following equation (Equation (2)) [78]:

$$\eta = b \cdot \log j/j_0 \quad (2)$$

where η is the overpotential, b is the Tafel slope, j is the experimental current density, and j_0 is the exchange current density. The plot of η versus log *j* represents the Tafel slope. It is widely accepted that HER proceeds by either the Volmer–Heyrovsky or Volmer–Tafel mechanisms, and, in alkaline media, it involves three main steps as shown in Equations (3)–(5) [61]:

$$* + H_2O + e^- \rightarrow *H_{ads} + OH^- \text{ (Volmer step)} \quad (3)$$

$$*H_{ads} + e^- + H_2O \rightarrow H_2 + OH^- + * \text{ (Heyrovsky step)} \quad (4)$$

$$2*H_{ads} \rightarrow H_2 + * \text{ (Tafel step)} \quad (5)$$

where H_{ads} denotes the H_2 adsorbed to the metal sites and * indicates the metal sites. The theoretical Tafel slopes in the aforementioned reaction steps are 120 mV dec^{-1}, 40 mV dec^{-1}, and 30 mV dec^{-1}, respectively. Figure 5b shows the Tafel slopes of the g-C_3N_4, $CoFe_2O_4$/g-C_3N_4, and Ag@$CoFe_2O_4$/g-C_3N_4 samples, thus pointing to the rate-determining step and the likely mechanism associated with electrocatalytic hydrogen generation. The Ag@$CoFe_2O_4$/g-C_3N_4 catalyst was found to have the lowest Tafel slope of 62.9 mV dec^{-1} compared to $CoFe_2O_4$/g-C_3N_4 (79.1 mV dec^{-1}) and g-C_3N_4 (182.3 mV dec^{-1}). This predicted the favorable HER kinetics that apply following the Volmer–Heyrovsky mechanism on $CoFe_2O_4$/g-C_3N_4 and Ag@$CoFe_2O_4$/g-C_3N_4.

Among the investigated catalysts, the lower E_{onset} of −0.161 V, a small overpotential of −259 mV at 10 mA cm^{-2}, and a low Tafel slope of 62.9 mV dec^{-1} in Ag@$CoFe_2O_4$/g-C_3N_4 indicated that the addition of Ag nanocubes to $CoFe_2O_4$/g-C_3N_4 increased the activity for HER.

Investigation of Electrocatalyst Activity for OER

The performance of catalysts for OER was further evaluated. Figure 8a,b presents the OER polarization curves and the corresponding Tafel slopes recorded in the g-C_3N_4, $CoFe_2O_4$/g-C_3N_4, and Ag@$CoFe_2O_4$/g-C_3N_4 at a slow scan rate of 2 mV s^{-1} in a 1 M KOH solution. The summarized data are also given in Table 2.

Table 2. Electrochemical parameters of the investigated catalysts toward OER in alkaline media.

Catalysts	E_{onset}, V at j = 0.1 mA cm^{-2}	η_{onset}, mV	E, V at j = 10 mA cm^{-2}	η_{10} *, mV	Tafel Slope, mV dec^{-1}
g-C_3N_4	1.6404	410.4	–	–	139.9
$CoFe_2O_4$/g-C_3N_4	1.5056	275.6	1.6127	382.7	52.3
Ag@$CoFe_2O_4$/g-C_3N_4	1.4855	255.5	1.6000	370.2	48.1

* Overpotential at 10 mA cm^{-2}.

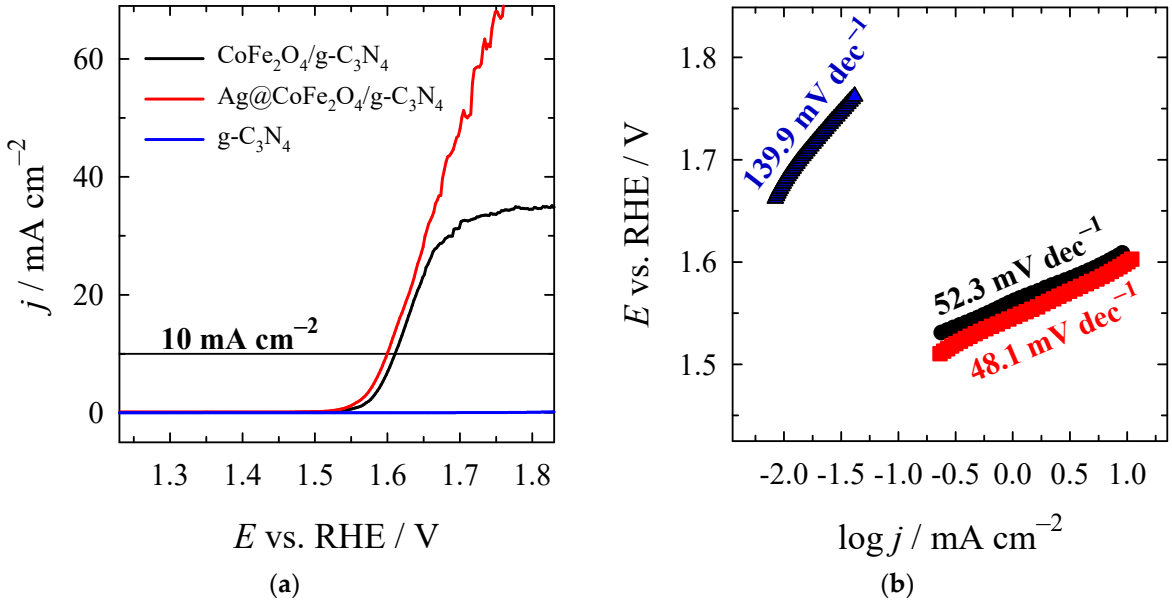


Figure 8. (**a**) OER polarization curves of the g-C_3N_4, $CoFe_2O_4$/g-C_3N_4, and Ag@$CoFe_2O_4$/g-C_3N_4 catalysts in a 1 M KOH solution at a potential scan rate of 2 mV s^{-1}. (**b**) The corresponding Tafel slopes for each catalyst.

Notably, pure g-C_3N_4 shows poor OER activity with a low current density, even at a high overpotential. On the contrary, $CoFe_2O_4$/g-C_3N_4 and Ag@$CoFe_2O_4$/g-C_3N_4 gave much higher current densities and lower overpotentials compared to g-C_3N_4, meaning a significant improvement for OER catalytic activity. E_{onset} values were found in a gradually increasing order as follows: Ag@$CoFe_2O_4$/g-C_3N_4 (1.4855 V) < $CoFe_2O_4$/g-C_3N_4 (1.5056 V) < g-C_3N_4 (1.6404 V). Furthermore, these had overpotential values of 255.5, 275.6, and 410.4 mV, respectively (Table 3). The overpotentials required to reach the current density of 10 mA·cm^{-2} were found as 370.2 and 382.7 mV for Ag@$CoFe_2O_4$/g-C_3N_4 and $CoFe_2O_4$/g-C_3N_4, respectively (Table 2). The Tafel slope of Ag@$CoFe_2O_4$/g-C_3N_4 (48.1 mV dec^{-1}) was lower than those of $CoFe_2O_4$ and g-C_3N_4 (Figure 8b, Table 2), indicating a better catalytic activity for the OER. A $4e^-$ mechanism was widely accepted for the OER process. The steps of the reaction in an alkaline media can be represented by Equations (6)–(9) [58,61,79]:

$$* + OH^- \rightarrow e^- + OH* \quad (6)$$

$$OH^- + OH* \rightarrow e^- + O* + H_2O \quad (7)$$

$$OH^- + O* \rightarrow e^- + OOH* \quad (8)$$

$$OH^- + OOH* \rightarrow H_2O + *+ e^- + O_2 \quad (9)$$

where * denotes the electrocatalyst's adsorption site. Similarly, the adsorbed intermediates were OH*, O*, and OOH* during OER. The first step of the OER process, denoted by Equation (6), was the electrosorption of OH^- onto the active sites of the catalyst's surface. Higher-oxidation-state metal species are more susceptible to adsorbing OH^-, thus they accelerate the multielectron transportation process; therefore, they can enhance the OER process [58,79].

Table 3. Electrochemical parameters of the different Co-based gC_3N_4 catalysts for HER and OER in alkaline media.

Catalyst	Electrolyte	HER		OER		Ref.
		η_{10} *, mV	Tafel Slope, mV dec^{-1}	η_{10} *, mV	Tafel Slope, mV dec^{-1}	
$CoFe_2O_4$/g-C_3N_4	1 M KOH	424.6	76.1	382.7	52.3	This study
Ag@$CoFe_2O_4$/g-C_3N_4	1 M KOH	259.0	62.9	370.2	48.1	This study
$CoFe_2O_4$/gCN/NGQDs	1 M KOH	287	96	445	69	[61]
Co_2FeO_4@rGO (CFG-10)	1 M KOH	320	48	240 at 20mA cm^{-2}	51	[6]
Co_2FeO_4@PdO	1 M KOH	269	49	259 at 20mA cm^{-2}	59	[80]
$CoNi_2S_4$/gCN	1 M KOH	160	90.76	310 at 30mA cm^{-2}	49.86	[81]
Co-SCN/RGO	1 M KOH	150	94	250	96	[82]
Co_3O_4/g-C_3N_4	1 M KOH	313	169	315	67	[83]
$Co_3O_4MoO_3$/g-C_3N_4	1 M KOH	125	94	206	60	[83]

* Overpotential at 10 mA cm^{-2}.

Additionally, the stability of the $CoFe_2O_4$/g-C_3N_4 and Ag@$CoFe_2O_4$/g-C_3N_4 catalysts was examined for 1000 cycles at a constant scan rate of 100 mV s^{-1}, and at a rotation rate of 1600 rpm in N_2-saturated 1 M KOH for HER and OER. Figure 9 presents the initial and after 1000 cycles LSVs that were recorded at 2 mV s^{-1} at 1600 rpm for both processes on the investigated materials. $CoFe_2O_4$/g-C_3N_4 exhibited a negligible shift of approximately 20 mV after 1000 potential cycles (Figure 9a), indicating good stability in alkaline media. In contrast, Ag@$CoFe_2O_4$/g-C_3N_4 showed a higher HER activity after 1000 cycles by the potential shift of approximately 17 mV to more positive potential values (Figure 9c). In the case of OER, the LSV curves for both catalysts exhibited almost no differences from the initial test before the CV cycles (Figure 9b,d) that occurred at a constant current density of 10 mA cm^{-2}, as well as at a minimal change of approximately 9 and 20 mV at 120 mA cm^{-2} for Ag@$CoFe_2O_4$/g-C_3N_4 and $CoFe_2O_4$/g-C_3N_4, respectively (which indicated high stability for OER). The obtained data show the potential of $CoFe_2O_4$/g-C_3N_4 and Ag@$CoFe_2O_4$/g-C_3N_4 catalysts for practical application.

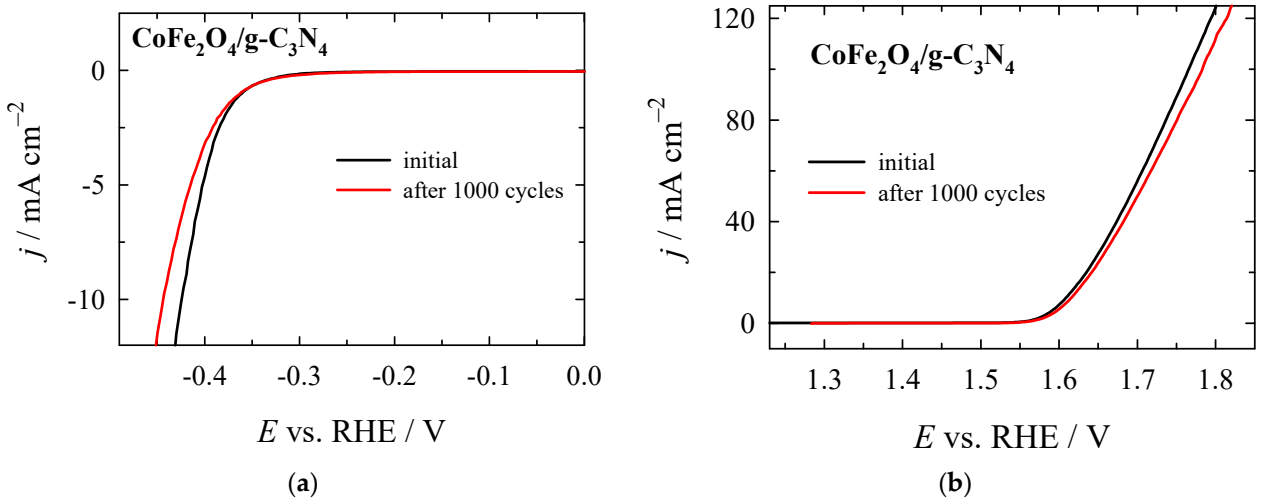


Figure 9. *Cont.*

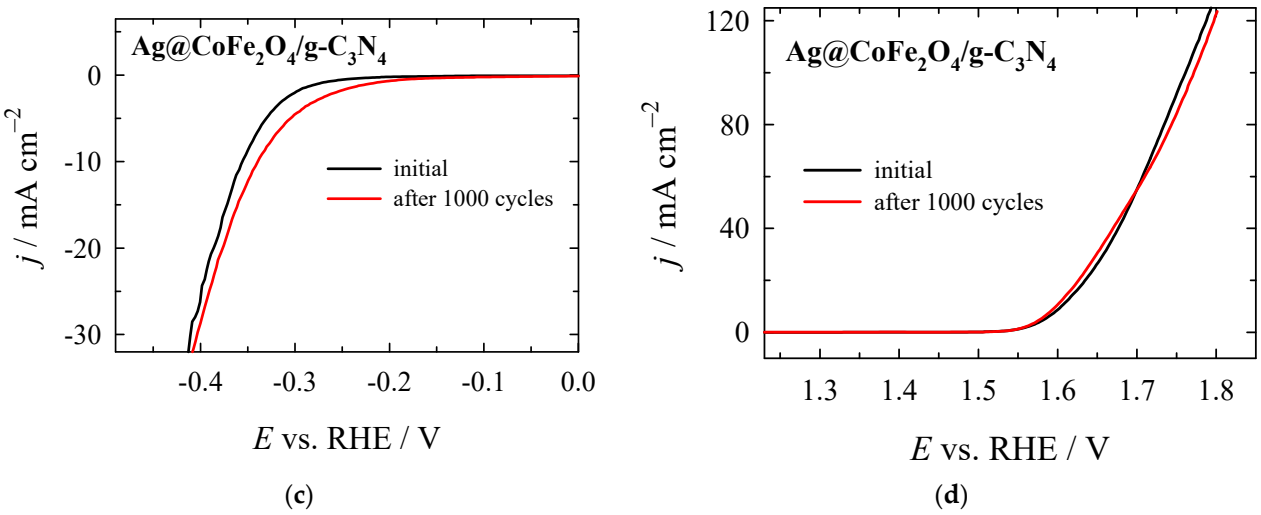


Figure 9. LSV curves before and after 1000 cycles for HER and OER for $CoFe_2O_4/g\text{-}C_3N_4$ (**a**,**b**) and $Ag@CoFe_2O_4/g\text{-}C_3N_4$, which were (**c**,**d**) recorded at 2 mV s^{-1} at 1600 rpm.

The above results demonstrated that $CoFe_2O_4/g\text{-}C_3N_4$ and $Ag@CoFe_2O_4/g\text{-}C_3N_4$ materials could act as bifunctional catalysts due to their notable performances and high stabilities toward HER and OER.

The catalytic activity of the $CoFe_2O_4/g\text{-}C_3N_4$ and $Ag@CoFe_2O_4/g\text{-}C_3N_4$ materials was also compared with previously reported works and is presented in Table 3. These overpotentials are comparable to those previously reported for state-of-the-art non-precious metal catalysts for water splitting in an alkaline medium. It was seen that $Ag@CoFe_2O_4/g\text{-}C_3N_4$ exhibited lower HER overpotential values at 10 mA cm^{-2} and a lower Tafel slope when compared to $CoFe_2O_4/gCN/NGQDs$ and $Co_3O_4/g\text{-}C_3N_4$, whereas the $CoNi_2S_4/gCN$, Co-SCN/RGO, and $Co_3O_4MoO_3/g\text{-}C_3N_4$ catalysts exhibited lower overpotential values but higher Tafel slopes. In the case of OER, $Ag@CoFe_2O_4/g\text{-}C_3N_4$ achieved a lower overpotential value at 10 mA cm^{-2} and a lower Tafel slope of 48.1 mV dec^{-1} compared to $CoFe_2O_4/gCN/NGQDs$, but it had lower overpotential values at 10 mA cm^{-2}. Meanwhile, higher Tafel slope values were exhibited by Co_2FeO_4@rGO (CFG-10), Co_2FeO_4@PdO, $CoNi_2S_4/gCN$, Co-SCN/RGO, $Co_3O_4/g\text{-}C_3N_4$, and $Co_3O_4MoO_3/g\text{-}C_3N_4$ when compared with those for $Ag@CoFe_2O_4/g\text{-}C_3N_4$.

4. Conclusions

In this study, we reported the synthesis of $CoFe_2O_4/g\text{-}C_3N_4$ and $Ag@CoFe_2O_4/g\text{-}C_3N_4$ nanostructures, which was achieved with the polyol method, as well as their employment as electrocatalysts for HER and OER in alkaline media. It was found that $Ag@CoFe_2O_4/g\text{-}C_3N_4$ shows the highest current density and gives the lowest overpotential of −259 mV for HER in terms of reaching a current density of 10 mA cm^{-2} in a 1 M KOH. The overpotentials for reaching the current density of 10 mA·cm^{-2} for OER were 370.2 mV and 382.7 mV for $Ag@CoFe_2O_4/g\text{-}C_3N_4$ and $CoFe_2O_4/g\text{-}C_3N_4$, respectively. The above results demonstrate that $CoFe_2O_4/g\text{-}C_3N_4$ and $Ag@CoFe_2O_4/g\text{-}C_3N_4$ materials could act as bifunctional catalysts due to their notable performances and high stabilities toward HER and OER.

Author Contributions: Conceptualization, A.Z., E.N. and L.T.-T.; methodology, R.L. and O.E.-L.; validation, R.L. and O.E.-L., data curation, D.S. and A.Z.; investigation, Z.K.; formal analysis, Z.K.; writing—original draft preparation, A.Z., D.S., R.L. and L.T.-T.; writing—review and editing, E.N., D.S. and A.Z.; supervision, A.Z. and E.N.; project administration, E.N. All authors have read and agreed to the published version of the manuscript.

Funding: This project received funding from the European Social Fund (project No. 09.3.3-LMT-K-712-23-0188) under a grant agreement with the Research Council of Lithuania (LMTLT).

Data Availability Statement: Not applicable.

Acknowledgments: The authors are grateful to Audrius Drabavičius from the Department of Characterization of Materials Structure, Center for Physical Sciences and Technology for their materials characterization via TEM.

Conflicts of Interest: The authors declare no conflict of interest.

Abbreviations

The following abbreviations were used in this manuscript:

$CoFe_2O_4$	Cobalt ferrite
EDS	Energy-dispersive X-ray analysis
E_{onset}	Onset potential
η_{onset}	Onset overpotential
g-C_3N_4	Graphitic carbon nitride
HER	Hydrogen evolution reaction
j	Current density (mA cm^{-2})
NHE	Normal hydrogen electrode
LSVs	Linear sweep voltammograms
PVP	Polyvinylpyrrolidone
OER	Oxygen evolution reaction
RHE	Reversible hydrogen electrode
SEM	Scanning electron microscopy
TEG	Tetra ethylene glycol
TEM	Transmission electron microscopy
XRD	X-ray diffraction

References

1. Gong, Y.; Yao, J.; Wang, P.; Li, Z.; Zhou, H.; Xu, C. Perspective of hydrogen energy and recent progress in electrocatalytic water splitting. *Chin. J. Chem. Eng.* **2022**, *43*, 282–296. [CrossRef]
2. Yu, Z.-Y.; Duan, Y.; Feng, X.-Y.; Yu, X.G.; Gao, M.-R.; Yu, S.-H. Clean and affordable hydrogen fuel from alkaline water splitting: Past, recent progress, and future prospects. *Adv. Mater.* **2021**, *33*, 2007100. [CrossRef]
3. Yao, Y.; Gao, X.; Meng, X. Recent advances on electrocatalytic and photocatalytic seawater splitting for hydrogen evolution. *Int. J. Hydrogen Energy* **2021**, *46*, 469087–469100. [CrossRef]
4. Li, L.G.; Wang, P.T.; Shao, Q.; Huang, X.Q. Metallic nanostructures with low dimensionality for electrochemical water splitting. *Chem. Soc. Rev.* **2020**, *49*, 3072–3106. [CrossRef]
5. You, B.; Sun, Y. Innovative strategies for electrocatalytic water splitting. *Acc. Chem. Res.* **2018**, *51*, 1571–1580. [CrossRef] [PubMed]
6. Hanan, A.; Shu, D.; Aftab, U.; Cao, D.; Laghari, A.J.; Solangi, M.Y.; Abro, M.I.; Nafady, A.; Vigolo, B.; Tahira, A.; et al. Co_2FeO_4@rGO composite: Towards trifunctional water splitting in alkaline media. *Int. J. Hydrogen Energy* **2022**, *47*, 33919–33937. [CrossRef]
7. Ng, K.H.; Lai, S.Y.; Cheng, C.K.; Cheng, Y.W.; Chong, C.C. Photocatalytic water splitting for solving energy crisis: Myth, Fact or Busted? *J.Chem. Eng.* **2021**, *417*, 128847. [CrossRef]
8. Zhang, H.; Fu, Y.; Nguyen, H.T.; Fox, B.; Lee, J.H.; Lau, A.K.-T.; Zheng, H.; Lin, H.; Ma, T.; Jis, B. Material challenges in green hydrogen ecosystem. *Coord. Chem. Rev.* **2023**, *494*, 215272. [CrossRef]
9. Zheng, D.; Xue, Y.; Wang, J.; Varbanov, P.S.; Klemeš, J.J.; Yin, C. Nanocatalysts in photocatalytic water splitting for green hydrogen generation: Challenges and opportunities. *J. Clean. Prod.* **2023**, *414*, 137700. [CrossRef]
10. Sun, H.; Meng, J.; Jiao, L.; Cheng, F.; Chen, J. A review of transition-metal boride/phosphide-based materials for catalytic hydrogen generation from hydrolysis of boron-hydrides. *Inorg. Chem. Front.* **2018**, *5*, 760. [CrossRef]
11. Dong, G.; Zhang, Y.; Pan, Q.; Qiu, J. A fantastic graphitic carbon nitride (g-C_3N_4) material: Electronic structure, photocatalytic and photoelectronic properties. *J. Photochem. Photobiol. C* **2014**, *20*, 33–50. [CrossRef]
12. Zhao, Z.; Sun, Y.; Dong, F. Graphitic carbon nitride based nanocomposites: A review. *Nanoscale* **2015**, *7*, 15–37. [CrossRef] [PubMed]
13. Suja, P.; John, J.; Rajan, T.P.D.; Anilkumar, G.M.; Yamaguchi, T.; Pillai, S.C.; Hareesh, U.S. Graphitic carbon nitride (g-C_3N_4) based heterogeneous single atom catalysts: Synthesis, characterisation and catalytic applications. *J. Mater. Chem. A* **2023**, *11*, 8599. [CrossRef]

14. Alaghmandfard, A.; Ghandi, K. A Comprehensive review of graphitic carbon nitride (g-C_3N_4)–metal oxide-based nanocomposites: Potential for photocatalysis and sensing. *Nanomaterials* **2022**, *12*, 294. [CrossRef] [PubMed]
15. Kalyani, A.K.M.; Rajeev, R.; Benny, L.; Cherian, A.R.; Varghese, A. Surface tuning of nanostructured graphitic carbon nitrides for enhanced electrocatalytic applications: A review. *Mater. Today Chem.* **2023**, *30*, 101523. [CrossRef]
16. Ismael, M. A review on graphitic carbon nitride (g-C_3N_4) based nanocomposites: Synthesis, categories, and their application in photocatalysis. *J. Alloys Compd.* **2020**, *846*, 156446. [CrossRef]
17. Molaei, M.J. Graphitic carbon nitride (g-C_3N_4) synthesis and heterostructures, principles, mechanisms, and recent advances: A critical review. *Int. J. Hydrogen Energy* **2023**, *in press*. [CrossRef]
18. Iqbal, O.; Ali, H.; Li, N.; Al-Sulami, A.I.; Alshammari, K.F.; Abd-Rabboh, H.S.M.; Al-Hadeethi, Y.; Ud Din, I.; Alharthi, A.I.; Altamimi, R.; et al. A review on the synthesis, properties, and characterizations of graphitic carbon nitride (g-C_3N_4) for energy conversion and storage applications. *Mater. Today Phys.* **2023**, *34*, 101080. [CrossRef]
19. Talukdar, M.; Deb, P. Recent progress in research on multifunctional graphitic carbon nitride: An emerging wonder material beyond catalyst. *Carbon* **2022**, *192*, 308–331. [CrossRef]
20. Govindaraju, V.R.; Sureshkumar, K.; Ramakrishnappa, T.; Muralikrishna, S.; Samrat, D.; Pai, R.K.; Kumar, V.; Vikrant, K.; Kim, K.H. Graphitic carbon nitride composites as electro catalysts: Applications in energy conversion/storage and sensing system. *J. Clean. Prod.* **2021**, *320*, 128693. [CrossRef]
21. Ajiboye, T.O.; Kuvarega, A.T.; Onwudiwe, D.C. Graphitic carbon nitride-based catalysts and their applications: A Review. *Nano-Struct. Nano-Objects* **2020**, *24*, 100577. [CrossRef]
22. Kong, L.; Wang, J.; Ma, F.; Sun, M.; Quan, J. Graphitic carbon nitride nanostructures: Catalysis. *Appl. Mater. Today* **2019**, *16*, 388–424. [CrossRef]
23. Besharat, F.; Ahmadpoor, F.; Nezafat, Z.; Nasrollahzadeh, M.; Manwar, N.R.; Fornasiero, P.; Gawande, M.B. Advances in carbon nitride-based materials and their electrocatalytic applications. *ACS Catal.* **2022**, *12*, 5605–5660. [CrossRef]
24. Darkwah, W.K.; Ao, Y. Mini review on the structure and properties (photocatalysis), and preparation techniques of graphitic carbon nitride nano-based particle, and its applications. *Nanoscale Res. Lett.* **2018**, *13*, 388. [CrossRef]
25. Wang, J.; Wang, S. A critical review on graphitic carbon nitride (g-C_3N_4)-based materials: Preparation, modification and environmental application. *Coord. Chem. Rev.* **2022**, *453*, 214338. [CrossRef]
26. Ye, S.; Wang, R.; Wu, M.-Z.; Yuan, Y.-P. A review on g-C_3N_4 for photocatalytic water splitting and CO_2 reduction. *Appl. Surf. Sci.* **2015**, *358*, 15–27. [CrossRef]
27. Martín-Ramos, P.; Martín-Gil, J.; Dante, R.C.; Vaquero, F.; Navarro, R.M.; Fierro, J.L.G. A simple approach to synthesize g-C_3N_4 with high visible light photoactivity for hydrogen production. *Int. J. Hydrogen Energy* **2015**, *40*, 7273–7281. [CrossRef]
28. Wudil, Y.S.; Ahmad, U.F.; Gondal, M.A.; Al-Osta, M.A.; Almohammedi, A.; Sa'id, R.S.; Hrahsheh, F.; Haruna, K.; Mohamed, M.J.S. Tuning of graphitic carbon nitride (g-C_3N_4) for photocatalysis: A critical review. *Arab. J. Chem.* **2023**, *16*, 104542. [CrossRef]
29. Singla, S.; Sharma, S.; Basu, S.; Shetti, N.P.; Aminabhavi, T.M. Photocatalytic water splitting hydrogen production via environmental benign carbon based nanomaterials. *Int. J. Hydrogen Energy* **2021**, *46*, 33696–33717. [CrossRef]
30. Sahani, S.; Tripathi, K.M.; Lee, T.I.; Dubal, D.P.; Wong, C.-P.; Sharma, Y.C.; Kim, T.Y. Recent advances in photocatalytic carbon-based materials for enhanced water splitting under visible-light irradiation. *Energy Convers. Manag.* **2022**, *252*, 115133. [CrossRef]
31. Al-Ahmed, A. Photocatalytic properties of graphitic carbon nitrides (g-C_3N_4) for sustainable green hydrogen production: Recent advancement. *Fuel* **2022**, *316*, 123381. [CrossRef]
32. Gupta, A.; Likozar, B.; Jana, R.; Chanu, W.C.; Singh, M.K. A review of hydrogen production processes by photocatalytic water splitting—From atomistic catalysis design to optimal reactor engineering. *Int. J. Hydrogen Energy* **2022**, *47*, 33282–33307. [CrossRef]
33. Nasir, M.S.; Yang, G.; Ayub, I.; Wang, S.; Wang, L.; Wang, X.; Yan, W.; Peng, S.; Ramakarishna, S. Recent development in graphitic carbon nitride based photocatalysis for hydrogen generation. *Appl. Catal. B* **2019**, *257*, 117855. [CrossRef]
34. Ye, J.; Banda, T.K.; Ajmal, Z.; Ahmed, J.; Raza, S.; Ghasali, E.; Hayat, A.; Orioji, Y. Organic conjugation of graphitic carbon nitride nanocomposites for boosted photocatalytic water splitting. *Mater. Sci. Semicond.* **2023**, *166*, 107742. [CrossRef]
35. Sharma, R.; Almáši, M.; Nehra, S.P.; Rao, V.S.; Panchal, P.; Paul, D.R.; Jain, I.P.; Sharma, A. Photocatalytic hydrogen production using graphitic carbon nitride (GCN): A precise review. *Renew. Sustain. Energy Rev.* **2022**, *168*, 112776. [CrossRef]
36. Wang, L.; Si, W.; Tong, Y.; Hou, F.; Pergolesi, D.; Hou, J.; Lippert, T.; Dou, S.X.; Liang, J. Graphitic carbon nitride (g-C_3N_4)-based nanosized heteroarrays: Promising materials for photoelectrochemical water splitting. *Carbon Energy.* **2020**, *2*, 223–250. [CrossRef]
37. Malik, R.; Tomer, V.K. State-of-the-art review of morphological advancements in graphitic carbon nitride (g-CN) for sustainable hydrogen production. *Renew. Sustain. Energy Rev.* **2021**, *135*, 110235. [CrossRef]
38. Sun, Y.; Kumar, V.; Kim, K.H. The assessment of graphitic carbon nitride (g-C_3N_4) materials for hydrogen evolution reaction: Effect of metallic and non-metallic modifications. *Sep. Purif. Technol.* **2023**, *305*, 122413. [CrossRef]
39. Thomas, A.; Fischer, A.; Goettmann, F.; Antonietti, M.; Müller, J.-O.; Schlügl, R.; Carlsson, J.M. Graphitic carbon nitride materials: Variation of structure and morphology and their use as metal-free catalysts. *J. Mater. Chem.* **2008**, *18*, 4893–4908. [CrossRef]
40. Kim, M.; Hwang, S.; Yu, J.S. Novel ordered nanoporous graphitic C_3N_4 as a support for Pt–Ru anode catalyst in direct methanol fuel cell. *J. Mater. Chem.* **2007**, *17*, 1656–1659.
41. Groenewolt, M.; Antonietti, M. Synthesis of g-C_3N_4 nanoparticles in mesoporous silica host matrices. *Adv. Mater.* **2005**, *17*, 1789–1792. [CrossRef]

42. Yan, S.C.; Li, Z.S.; Zou, Z.G. Photodegradation performance of g-C_3N_4 fabricated by directly heating melamine. *Langmuir* **2009**, *25*, 10397–10401. [CrossRef] [PubMed]
43. Li, X.; Zhang, J.; Shen, L.; Ma, Y.; Lei, W.; Cui, Q.; Zou, G. Preparation and characterization of graphitic carbon nitride through pyrolysis of melamine. *Appl. Phys. A* **2009**, *94*, 387–392. [CrossRef]
44. Gu, Q.; Gao, Z.; Zhao, H.; Lou, Z.; Liao, Y.; Xue, C. Temperature-controlled morphology evolution of graphitic carbon nitride nanostructures and their photocatalytic activities under visible light. *RSC Adv.* **2015**, *5*, 49317–49325. [CrossRef]
45. Zhou, L.; Guo, S. Noble metal-free electrocatalytic materials for water splitting in alkaline electrolyte. *EnergyChem* **2021**, *3*, 100053. [CrossRef]
46. Li, S.; Li, E.; An, X.; Hao, X.; Jiange, Z.; Guan, G. Transition metal-based catalysts for electrochemical water splitting at high current density: Current status and perspectives. *Nanoscale* **2021**, *13*, 12788–127817. [CrossRef] [PubMed]
47. Wu, H.; Feng, C.; Zhang, L.; Zhang, J.; Wilkinson, D.P. Non-noble metal electrocatalysts for the hydrogen evolution reaction in water electrolysis. *Electrochem. Energy Rev.* **2021**, *4*, 473–507. [CrossRef]
48. Al-Naggar, A.H.; Shinde, N.M.; Kim, J.-S.; Mane, R.S. Water splitting performance of metal and non-metal-doped transition metal oxide electrocatalysts. *Coord. Chem. Rev.* **2023**, *474*, 214864. [CrossRef]
49. Chen, Z.; Wei, W.; Ni, B.-J. Cost-effective catalysts for renewable hydrogel production via electrochemical water splitting: Recent advances. *Curr. Opin. Green Sustain. Chem.* **2021**, *27*, 100398. [CrossRef]
50. Du, P.; Eisenberg, R. Catalysts made of earth-abundant elements (Co, Ni, Fe) for water splitting: Recent progress and future challenges. *Energy Environ. Sci.* **2012**, *5*, 6012–6021. [CrossRef]
51. Cao, X.; Wang, T.; Jiao, L. Transition-metal (Fe, Co, and Ni)-based nanofiber electrocatalysts for water splitting. *Adv. Fiber Mater.* **2021**, *3*, 210–228. [CrossRef]
52. Han, L.; Dong, S.; Wang, E. Transition-metal (Co, Ni, and Fe)-based electrocatalysts for the water oxidation reaction. *Adv. Mater.* **2016**, *28*, 9266–9291. [CrossRef] [PubMed]
53. Liu, D.; Ai, H.; Chen, M.; Zhou, P.; Li, B.; Liu, D.; Du, X.; Lo, K.H.; Ng, K.W.; Wang, S.P.; et al. Multi-phase heterostructure of CoNiP/Co_xP for enhanced hydrogel evolution under alkaline and seawater conditions by promoting H_2O dissociation. *Small* **2021**, *17*, 2007557. [CrossRef]
54. Jung, H.; Ma, A.; Abbas, S.A.; Kim, H.Y.; Choe, H.R.; Jo, S.Y.; Nam, K.M. A new synthetic approach to cobalt oxides: Designed phase transformation for electrochemical water splitting. *Chem. Eng. J.* **2021**, *415*, 127958. [CrossRef]
55. Duraivel, M.; Nagappan, S.; Park, K.H.; Prabakar, K. Hierarchical 3D flower like cobalt hydroxide as an efficient bifunctional electrocatalyst for water splitting. *Electrochim. Acta* **2022**, *411*, 140071. [CrossRef]
56. Xue, Z.; Kang, J.; Guo, D.; Zhu, C.; Li, C.; Zhang, X.; Chen, Y. Self-supported cobalt nitride porous nanowire arrays as bi-functional electrocatalyst for overall water splitting. *Electrochim. Acta* **2018**, *273*, 229–238. [CrossRef]
57. Zou, H.; Li, G.; Duan, L.; Kou, Z.; Wang, J. In situ coupled amorphous cobalt nitride with nitrogen-doped graphene aerogel as a trifunctional electrocatalyst towards Zn-air battery deriven full water splitting. *Appl. Catal. B Environm.* **2019**, *259*, 118100. [CrossRef]
58. Bian, H.; Chen, T.; Chen, Z.; Liu, J.; Li, Z.; Du, P.; Zhou, B.; Zeng, X.; Tang, J.; Liu, C. One-step synthesis of mesoporous cobalt sulfides (CoS_x) on the metal substrate as an efficient bifunctional electrode for overall water splitting. *Electrochim. Acta* **2021**, *389*, 138786. [CrossRef]
59. Wu, Y.; Wang, F.; Ke, N.; Dong, B.; Huang, A.; Tan, C.; Yin, L.; Xu, X.; Hao, L.; Xian, Y.; et al. Self-supported cobalt/cobalt selenide heterojunction for highly efficient overall water splitting. *J. Alloys Compd.* **2022**, *925*, 166683. [CrossRef]
60. Wang, Q.; He, R.; Yang, F.; Tian, X.; Sui, H.; Feng, L. An overview of heteroatom doped cobalt phosphide for efficient electrochemical water splitting. *Chem. Eng. J.* **2023**, *456*, 141056. [CrossRef]
61. Reghunath, B.S.; Rajasekaran, S.; Devi, K.R.S.; Pinheiro, D.; Jaleel UC, J.R. N-doped graphene quantum dots incorporated cobalt ferrite/graphitic carbon nitride ternary composite for electrochemical overall water splitting. *Int. J. Hydrogen Energy* **2023**, *48*, 2906–2919. [CrossRef]
62. Haase, F.T.; Rabe, A.; Schmidt, F.-P.; Herzog, A.; Jeon, H.S.; Frandsen, W.; Narangoda, P.V.; Spanos, I.; Ortega, K.F.; Timoshenko, J.; et al. Role of nanoscale inhomogeneities in Co_2FeO_4 catalysts during the oxygen evolution reaction. *J. Am. Chem. Soc.* **2022**, *144*, 12007–12019. [CrossRef]
63. Huang, C.; Qin, P.; Luo, Y.; Ruan, Q.; Liu, L.; Wu, Y.; Li, Q.; Xu, Y.; Liu, R.; Chu, P.K. Recent progress and perspective of cobalt-based catalysts for water splitting: Design and nanoarchitectonics. *Mater. Today Energy* **2022**, *23*, 10091. [CrossRef]
64. Zhang, W.; Cui, L.; Liu, J. Recent advances in cobalt-based electrocatalysts for hydrogen and oxygen evolution reactions. *J. Alloys Compd.* **2020**, *821*, 153542. [CrossRef]
65. Paul, A.; Dhar, S.S. Designing $Cu_2V_2O_7$/$CoFe_2O_4$/g-C_3N_4 ternary nanocomposite: A high performance magnetically recyclable photocatalyst in the reduction of 4-nitrophenol to 4-aminophenol. *J. Solid State Chem.* **2020**, *290*, 121563. [CrossRef]
66. He, G.; Wen, Y.; Ma, C.; Li, X.; Gao, L.; Sun, Z. Photocatalytic hydrogen evolution of nanoporous $CoFe_2O_4$ and $NiFe_2O_4$ for water splitting. *Int. J. Hydrogen Energy* **2021**, *46*, 5369–5377. [CrossRef]
67. Feng, C.; Lu, Z.; Zhang, Y.; Liang, Q.; Zhou, M.; Li, X.; Yao, C.; Li, Z.; Xu, S. A magnetically recyclable dual Z-scheme GCNQDs-$CoTiO_3$/$CoFe_2O_4$ composite photocatalyst for efficient photocatalytic degradation of oxytetracycline. *J. Chem. Eng.* **2022**, *435*, 134833. [CrossRef]

68. Yesmin, S.; Devi, M.; Dasgupta, R.; Dhar, S.S. $CoFe_2O_4$ nanocubes over Cu/graphitic carbon nitride as electrode materials for solid-state asymmetric supercapacitors. *J. Chem. Eng.* **2022**, *446*, 136540. [CrossRef]
69. Ren, T.; Liu, Y.; Shi, C.; Li, C. Bimetal-organic framework-derived porous $CoFe_2O_4$ nanoparticles as biocompatible anode electrocatalysts for improving the power generation of microbial fuel cells. *J. Colloid Interface Sci.* **2023**, *643*, 428–436. [CrossRef]
70. Xu, X.; Liu, M.; Nie, Y.; Wang, C.; Wang, W.; Liu, C.; Wang, X.; Cai, Z.; Liu, X.; Huo, S.; et al. Modulating electronic structure of interfacial Fe sites in $Fe_2N/CoFe_2O_4$ nano-heterostructure for enhancing corrosion-resistance and oxygen electrocatalysis in zinc-air batery. *J. Chem. Eng.* **2023**, *471*, 144639. [CrossRef]
71. Benedet, M.; Rizzi, G.A.; Gasparotto, A.; Gauquelin, N.; Orekhov, A.; Verbeeck, J.; Maccato, C.; Barreca, D. Functionalization of graphitic carbon nitride systems by cobalt and cobalt-iron oxides boosts solar water oxidation performances. *Appl. Surf. Sci.* **2023**, *618*, 156652. [CrossRef]
72. Hou, Y.; Liu, Y.; Gao, R.; Li, Q.; Guo, H.; Goswami, A.; Zboril, R.; Gawande, M.B.; Zou, X. Ag@CoxP core-shell heterogeneous nanoparticles as efficient oxygen evolution reaction catalysts. *ACS Catal.* **2017**, *7*, 7038–7042. [CrossRef]
73. Shafi, A.; Bano, S.; Sharma, L.; Halder, A.; Sabir, S.; Khan, M.Z. Exploring multifunctional behaviour of g-C_3N_4 decorated $BiVO_4/Ag_2CO_3$ hierarchical nanocomposite for simultaneous electrochemical detection of two nitroaromatic compounds and water splitting applications. *Talanta* **2022**, *241*, 123257. [CrossRef] [PubMed]
74. Bellamkonda, S.; Chakma, C.; Guru, S.; Neppolian, B.; Rao, G.R. Rational design of plasmonic $Ag@CoFe_2O_4/g\text{-}C_3N_4$ p-n heterojunction photocatalysts for efficient overall water splitting. *Int. J. Hydrogen Energy* **2022**, *47*, 18708–18724. [CrossRef]
75. Tao, A.; Sinsermsuksakul, P.; Yang, P. Polyhedral silver nanocrystals with distinct scattering signatures. *Angew. Chem. Int. Ed.* **2006**, *45*, 4597–4601. [CrossRef] [PubMed]
76. Hu, C.; Chu, Y.-C.; Wang, M.-S.; Wu, X.-H. Rapid synthesis of g-C_3N_4 spheres using microwave-assisted solvothermal method for enhanced photocatalytic activity. *J. Photochem. Photobiol. A Chem.* **2017**, *348*, 8–17. [CrossRef]
77. Sun, B.-W.; Yu, H.-Y.; Yang, Y.-J.; Li, H.-J.; Zhai, C.-Y.; Qian, D.-J.; Chen, M. New complete assignment of X-ray powder diffraction patterns in graphitic carbon nitride using discrete Fourier transform and direct experimental evidence. *Phys. Chem. Chem. Phys.* **2017**, *19*, 26072–26084. [CrossRef]
78. Zhu, G.X.; Lu, T.L.; Han, L.; Zhan, Y.Z. Graphitic carbon nitride (g–C_3N_4) as an efficient metal-free Fenton-like catalyst for degrading organic pollutants: The overlooked non-photocatalytic activity. *Water Sci. Technol.* **2020**, *81*, 518–528. [CrossRef]
79. Plevová, M.; Hnát, J.; Bouzek, K. Electrocatalysts for the oxygen evolution reaction in alkaline and neutral media. A comparative review. *J. Power Sources* **2021**, *507*, 230072. [CrossRef]
80. Hanan, A.; Lakhan, M.N.; Shu, D.; Hussain, A.; Ahmed, M.; Soomro, I.A.; Kumar, V.; Cao, D. An efficient and durable bifunctional electrocatalysts based on PdO and Co_2FeO_4 for HER and OER. *Int. J. Hydrogen Energy* **2023**, *48*, 19494–19508. [CrossRef]
81. Zahra, R.; Pervaiz, E.; Baig, M.M.; Rabi, O. Three-dimensional hierarchical flowers-like cobalt-nickel sulfide constructed on graphitic carbon nitride: Bifunctional non-noble electrocatalyst for overall water splitting. *Electrochim. Acta* **2022**, *418*, 140346. [CrossRef]
82. Jo, W.-K.; Moru, S.; Tonda, S. Cobalt-coordinated sulfur-doped graphitic carbon nitride on reduced graphene oxide: An efficient metal−(N,S)−C-class bifunctional electrocatalyst for overall water splitting in alkaline media. *ACS Sustain. Chem. Eng.* **2019**, *7*, 15373–15384. [CrossRef]
83. Ahmed, I.; Biswas, R.; Patil, R.A.; Halder, K.K.; Singh, H.; Banerjee, B.; Kumar, B.; Ma, Y.-R.; Haldar, K.K. Graphitic carbon nitride composites with MoO_3-decorated Co_3O_4 nanorods as catalysts for oxygen and hydrogen evolution. *ACS Appl. Nano Mater.* **2021**, *4*, 12672–12681. [CrossRef]

Disclaimer/Publisher's Note: The statements, opinions and data contained in all publications are solely those of the individual author(s) and contributor(s) and not of MDPI and/or the editor(s). MDPI and/or the editor(s) disclaim responsibility for any injury to people or property resulting from any ideas, methods, instructions or products referred to in the content.